Volume 16, Issue 2, 162509 (1-17)

International Journal of Nano Dimension (IJND)

https://doi.org/10.57647/j.ijnd.2025.1602.09

Formulation, interaction analysis, and invitro hepatocellular carcinoma studies of Rutin loaded lipid and polymeric nanoparticles

Mohammad Habeeb[1,2], Manimaran Vasanthan[1,*]

[1]*Department of Pharmaceutics, SRM College of Pharmacy, SRM Institute of Science and Technology, Kattankulathur, India.*
[2]*Department of Pharmaceutics, Crescent School of Pharmacy, B.S. Abdur Rahman Crescent Institute of Science and Technology, Chennai, India.*

[*]**Corresponding author:** manimarv@srmist.edu.in

Original Research

Received:
24 August 2024
Revised:
29 November 2024
Accepted:
2 December 2024
Published online:
1 April 2025

Abstract:

Hepatocellular carcinoma is a primary liver cancer with a high mortality rate worldwide. The limited efficacy and adverse effects of conventional chemotherapy have driven the exploration of novel therapeutic approaches, including Nano medicine-based anticancer agents. In this study, the best molecule was identified based on molecular-level interaction studies with the three anticancer pathway proteins. The best molecule was encapsulated with polymer and lipid to form nanoparticles and In vitro Hepatocellular carcinoma studies were performed to measure the activity. The interaction analysis revealed that Rutin binds effectively with all three proteins: folate receptor (5IZQ), vascular endothelial growth factor (5ABD), and CD44 (4PZ3), exhibiting binding energies of -44.5015 kcal/mol, -46.8331 kcal/mol, and -42.6949 kcal/mol, respectively. These results indicate that Rutin demonstrates stronger binding affinity compared to other anticancer agents by computation studies. In the formulation, Rutin-formed lipid nanoparticles exhibited higher encapsulation efficacy and drug-loading efficiency compared to polymeric nanoparticles. Dissolution studies of rutin-loaded lipid nanoparticles reveal a gradual release profile, reaching approximately 99% over 6 hours. This sustained release ensures extended drug activity within the tumor environment, improving therapeutic effectiveness. In vitro cytotoxicity studies demonstrated that Rutin-lipid nanoparticles had superior anticancer efficacy, with an IC50 value of 80.45 $\pm$ 0.05 μg/mL, compared to 120.45 $\pm$ 0.05 μg/mL for Rutin-polymeric nanoparticles against the Hep3B cell lines. Similarly, Fluorescence-based screening studies further confirmed the remarkable anti-cancer potential of Rutin-lipid nanoparticles, primarily by inducing apoptosis in Hep3B cells. These findings suggest that Rutin-lipid nanoparticles hold promise nano-formulations for targeting Hepatocellular carcinoma.

Keywords: Chemotherapy; Docking; Fluorescent cell studies; Hepatocellular carcinoma; Solid-Lipid nanoparticle

1. Introduction

Hepatocellular carcinoma (HCC) is a highly prevalent and deadly condition on a global scale, accounting for 85% of all liver cancer instances [1]. This disease is linked to substantial morbidity and mortality [2]. While cirrhosis is a primary risk factor for liver cancer, chronic infections with hepatitis B and hepatitis C viruses are widely recognized as significant factors contributing to the development of HCC [3]. Furthermore, exposure to harmful substances, alcohol intake, consumption of tainted foods, and the presence of metabolic disorders such as non-alcoholic fatty liver disease have also played a role in the onset of HCC [4]. At the cellular level, the pathogenesis of HCC is complex and involves multiple molecular abnormalities, including disruptions in the cell cycle, chromosomal instability, modulation of the immune response, transition of epithelial cells to a mesenchymal state, dysregulation of microRNAs, and an increase in the population of HCC stem cells. Rutin (RT) is a natural flavonoid found in medicinal herbs and is known for its potent antioxidant, anti-inflammatory, and anticancer possessions [5]. It has demonstrated therapeutic potential in various types of cancer, including liver cancer, primarily due to its strong antioxidant capabilities [6]. How-

ever, a significant limitation is its poor solubility in water and low oral absorption, which hinders its effectiveness in cancer treatment. Recently, advancements in nanotechnology have led to the development of nanoparticles (NPs), which have become increasingly valuable in the fields of biology and medicine [7]. These NPs are solid, spherical structures with a size of approximately 100 nm and are considered submicron-sized colloidal particles [8]. Solid lipid nanoparticles (SLNs) are a type of lipid-based nanocarrier with a solid core that can accommodate both hydrophilic and hydrophobic drugs. They are typically composed of biocompatible materials [9]. Solid colloidal drug delivery systems offer several advantages, including controlled drug release, prevention of drug leakage, low toxicity, and excellent biocompatibility [10]. Furthermore, prior research has demonstrated that SLNs have the potential to enhance drug bioavailability by influencing drug dissolution and can be employed to enhance the distribution of drugs within tissues. The literature discusses the use of different polymers for making polymeric nanoparticles, and among them, copolymers like PURASORB PDLG 5002A, which is a GMP-grade copolymer composed of equal parts of DL-lactide and glycolide, terminated with carboxylic acid, with an inherent viscosity midpoint of 0.2 dl/g in a 50/50 molar ratio, have gained attention [11]. PDLG nanoparticles are recognized for their ability to augment the solubility and stability of drugs. They can biodegrade into lactic acid and glycolic acid monomers, which are further metabolized by the body through the Krebs cycle and eliminated as carbon dioxide and water [12]. Consequently, they have very low systemic toxicity in biological systems. Various pieces of literature highlight the use of PDLG nanoparticles for encapsulating different anticancer drugs and their efficacious delivery, both in vitro and in vivo settings [13, 14]. Molecular docking and dynamics studies are computational methods cast off to forecast the binding of small molecules, such as drugs, to explicit receptors on the surface of cells [15–23]. In the context of hepatocellular carcinoma (HCC), these studies can be used to identify potential new drug targets for treating this type of liver cancer [24, 25]. Docking simulations predict the binding of a small molecule to a receptor by analyzing the interactions between the atoms of the molecule and the receptor [26–29]. Dynamics studies, on the other hand, can be used to predict how the molecule and receptor interact over time. Together, these techniques can provide important information about the potential efficacy and safety of new drugs for treating HCC [30, 31]. The importance of conducting this research lies in its potential to significantly advance the treatment of hepatocellular carcinoma (HCC), a leading cause of cancer-related deaths worldwide [26]. HCC, accounting for 85% of all liver cancer cases, is associated with high morbidity and mortality rates, and current treatment options, particularly in advanced stages, are limited [27]. This research is crucial for addressing this global health challenge by exploring the therapeutic potential of rutin, a natural flavonoid with strong antioxidant, anti-inflammatory, and anticancer properties. However, rutin's poor solubility and low oral absorption limit its clinical effectiveness, making it essential to develop advanced drug delivery systems that enhance its bioavailability [28]. Nanotechnology offers a promising solution, with nanoparticles such as solid lipid nanoparticles (SLNs) and polymeric nanoparticles improving the solubility, stability, and controlled release of drugs. By investigating rutin-loaded lipid and polymeric nanoformulations, this research aims to develop more effective and targeted therapies for HCC. Additionally, molecular docking and dynamics studies provide insights into drug-receptor interactions, helping to identify new drug targets and optimize nanoparticle-based delivery systems. This research not only bridges the gap between theoretical predictions and practical applications but also contributes to the development of personalized medicine by tailoring treatments to the specific molecular characteristics of a patient's cancer [29]. Ultimately, the findings from this study could pave the way for future research in cancer nanomedicine, inspiring further exploration of natural compounds and nanotechnology-based approaches in oncology. This research aims to compare molecular interaction, the design of the rutin-loaded lipid and polymeric nanoformulations and to assess the invitro consequences.

2. Materials and methods

2.1 Gathering of small molecules and protein

The objective of this investigation with the gather natural and synthetic active agents applied for targeting HCC. A total of 8 active agents illustrated in (Table 1) were gathered from the PubChem database https://pubchem.ncbi.nlm.nih.gov/ as .sdf file and it is converted as a 3D coordinated file using the BIOVIA discovery studio v 2021. Further, the target HCC disease proteins CD44 (4PZ3), folate receptors (5IZQ), and (5ABD-VEGF) were transferred from the RCSB database https://www.rcsb.org/ in a gz set-up [30]. This secondary, crystal structure of the human CD44 hyaluronan binding domain (PDB ID: 4PZ3) of the protein, the crystal structure of the human folate receptor alpha domain (PDB ID: 5IZQ), and the crystal structure of human VEGFR-1 DOMAIN 2 (PDB ID: VEGF) was fitted in the graphical space of the Discovery studio software and exposed for the energy minimization progression [31].

2.2 Refine and minimize the protein and ligand through optimization

Fewer energy molecules are only constant in nature as well as in our bodies. It was decided to use CHARMm and a smart minimizer method to achieve the stability of molecules and proteins. The initial potential energy and RMS of the molecule and the protein are calculated by the force field. The smart minimizer also employs two algorithms: steepest descent and conjugated gradient. These algorithms finish the parameter mentioned in (Table 2) and reduce energy at the atomic level [32].

2.3 Software and c-docker modules

To study the atomic level interaction pattern between the micro molecules and proteins, Discovery Studio v17 simulation software was used. Minimization and C-Docker mod-

Table 1. Structure of different anticancer agents intended for HCC.

Name of anticancer agents	Chemical Structure	Name of anticancer agents	Chemical Structure
Sorafenib	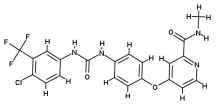	Regorafenib	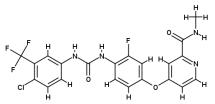
Quercetin	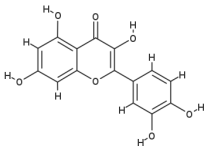	Curcumin	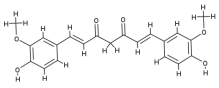
Resveratrol	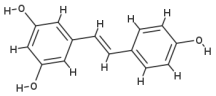	Hesperidin	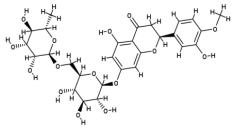
Rutin	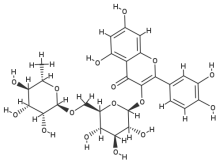	Lenvatinib	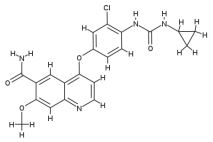

ules were used to study the complete interpretation of the interaction and energies of the complex [33]. As a start, the CHARMm force field was applied to 8 ligands, (Collected from PubChem) and three proteins (folate receptor 5IZQ, 5ABD-VEGF, and CD44 - 4PZ3) in the pre-preparation of docking to calculate potential energy and correct the errors in atomic levels [34]. In the second step, the energy of molecules was minimized to local minima using the smart minimizer algorithm of the spherical cut-off method with the 5000 maximum steps, 0.1 RMS gradient, and 14.0 ^{O}A non-bonded radius shown in (Table 3). Further, the active site of the protein was selected based on the PDB site record. The c-docker module algorithm was used with the following conditions to predict the best binding molecule with the various proteins.

2.4 Molecular dynamics studies

The stability of Rutin docked complex of (CD44- 4PZ3), (folate receptors -5IZQ), and (5ABD-VEGF) was investigated using Desmond module of Schrodinger 2021-4 by performing a 100 (ns), with a recording trajectory interval of 100 (ps) and 1000 number of confirmations was generated and analyzed. NPT ensemble was used with temperature 300k and pressure of 1.03215 bar. RESPA integrator times step was kept at 2.0 (fs) with coulombic interaction cut-off the radius of 9 ^{O}A. MD (Guo et al., 2010) simulation study. The composite in the explicit solvent structure with an OPLS3 force field was studied using the Desmond module of Schrodinger 2021-4 [35].

Table 2. Represents the Parameter setup for the Energy minimization.

Name of the Parameter	Setup value
Input Ligands	Molecules
Input force field	CHARMm
Minimization Algorithm	Smart Minimizer
Max Steps	2000
RMS Gradient	0.01
Dielectric Constant	1
Nonbond List Radius	18.0
Partial Charge Estimation	Momany-Rone

3. Materials

Purasorb PDLG 5002 A, a copolymer composed of carboxylic acid-terminated 50:50 DL-lactide: glycolide with an inherent viscosity midpoint of 0.2 dl/g, was generously provided by Corbion Purac in Amsterdam, The Netherlands. This copolymer was used in the production of nanoparticles. Various other materials, including PVA (with a molecular weight range of 30,000–70,000 and 87–90% hydrolysis ” Polysorbate 80, as well as acetone, and phosphate-buffered saline (PBS), were procured from Sigma Aldrich located in St. Louis, MO, USA.” Emulsifiers Compritol® 888 and Gelucire® 50/13, as well as co-emulsifier Labrafil®

Table 3. Represents parameters and setting for the C-Docker protocol settings for docking.

Protocol	Setting
Input receptor	5IZQ, 5ABD, 4PZ3
Input ligands	biomolecules
Top selection	10
Pose cluster radius	0.1
Random conformations	10
Molecular dynamics steps	1000
Target temperature	1000
Incorporate electrostatic interactions	TRUE
Orientations for refinement	10
Maximum unfavorable orientations	800
vdW energy threshold for orientation	300

M2125CS, were obtained as a gift sample from Gattefosse in Saint-Priest, France. Rutin (RT) was procured from Carbanio suppliers. The HCC cell lines Hep 3B, acquired from the American Type Culture Collection (ATCC) in Manassas, VA, were cultured in a minimal essential medium (MEM). All culture media were accompanied by 10% fetal bovine serum (FBS), penicillin (100 units/mL), and streptomycin (100 μg/mL), and the cells were maintained in a humid environment at 37 ^{O}C with 5% CO_2.

3.1 Preparation of Rutin-loaded polymeric nanoparticles (RTPNs)

A mixture of 5 to 10 mg of Purasorb® PDLG 5002 A and 0.5 to 4 mg of Rutin was liquefied in 0.5 to 1.0 mL of acetone while being stirred using a magnetic stirrer. A water phase, ranging from 2.0 to 4.0 mL in volume, was prepared with an aqueous solution (0.5 to 2.0% w/v) containing emulsifying agents like polysorbate 80 and poly (methacrylic acid sodium salt). This water phase was added all at once to the organic phase. Subsequently, the organic solvent was allowed to evaporate at room temperature and 1 bar pressure with continuous stirring over a 12-hour period. The resulting nanoparticles were then subjected to centrifugation (Eppendorf 5424 R, Hamburg, Germany) for 25 minutes, washed three times, and redispersed in an identical capacity of purified water [36].

3.2 Preparations of Rutin-loaded solid lipid nanoparticles (RTSLNs)

The production of RTSLN was accomplished using the high-energy, in this method separate aqueous and oil phases were fabricated. The oil phase, consisting of Compritol (1500 mg), labrafil (150 mg), Gelucire (1350 mg), and Rutin 60 mg, was heated and maintained at 80 ^{O}C until complete melting. Concurrently, the aqueous phase (20 mL of PBS) was gradually added to the oil part at the equivalent temperature (80 ^{O}C) while vigorously stirring at 10,000 rpm for 10 minutes using an Ultra-Turrax T25 (IKAWerke, Saufen, Germany). The resulting product was ultimately dispersed in PBS and further homogenized or subjected to sonication with a solvent [37].

3.3 Morphology estimate using transmission electron microscopy (TEM) analysis

Morphological analysis of RTSLNs and RTPNs was carried out using Transmission Electron Microscopy (TEM) at the central instrumentation facility (SCIF) of SRM Institute of Science and Technology in Chennai, India. To prepare the samples for TEM evaluation, a drop of the sample was appropriately diluted (1:20) in dual distilled water and sited on a copper grid layered with a membrane. Subsequently allowing the surplus liquid to drain, the system was left to air-dry at room temperature. Subsequently, the nanoformulations were examined using High-Resolution Transmission Electron Microscopy (HR-TEM) with a JEOL-JEM 2100 Plus instrument in Tokyo, Japan [38].

3.4 Measurement of the hydrodynamic size (HD), polydispersity index (PDI), and zeta potential

The hydrodynamic diameter, polydispersity index, and zeta potential of RTPNs and RTSLNs were assessed over a 120-day period using Dynamic Light Scattering (DLS) with a Zeta Sizer (Nano ZS, Malvern Instruments, UK) at 25 ^{O}C. These dimensions were conceded subsequently the tasters were diluted with distilled water at a 1:20 ratio [39].

3.5 Drug entrapment efficiency and drug loading

To find out the drug entrapment efficiency, percent entrapment efficiency (% EE) and percent drug loading (% DL) were found. The developed nano-formulations were evaluated by centrifuging the sample at 30 ^{O}C and 15000 rpm for 30 min. After centrifugation, the free amount of SFB present in the supernatant was determined by UV-Vis spectrophotometer at 257 nm. The following equations were used for %EE and %DL for the nano-formulations of RTPLNs and RTSLNs [40].

$$\text{Entrapment efficiency}(EE\%) = \frac{\text{Weight of RT in Nano-formulations}}{\text{Weight of RT used in Nano-formulations}} \times 100$$

$$\text{Drug loading}(DL\%) = = \frac{\text{Weight of RT in Nano-formulations}}{\text{Weight of Nano-formulations}} \times 100$$

3.6 Fourier transform infrared spectroscopy (FTIR)

The alterations in the functional clusters of the samples were examined through Fourier transform-infrared spectroscopy (JASCO 6300) at the central instrumentation facility of Crescent Institute of Science and Technology in Chennai, India. FTIR spectra for PDLG 5002 A, Compritol 888, RT, RTPLNs, and RTSLNs were acquired using the ATR (attenuated total reflections) method. The FTIR spectra were composed over the 4000–400 cm^{-1} range with a resolution of 4 cm^{-1}, averaging 50 scans [41].

3.7 In vitro drug release

To assess the drug liberation of encapsulated NP solutions of RTPNs and RTSLNs (each with a volume of 10 mL) containing an equivalent concentration of 0.1 mg/mL, they were subjected to dialysis in phosphate-buffered saline (PBS, 50 mL, pH 7.4, with 0.2% Tween 80). Dialysis was carried out using tubes with a molecular weight cutoff of 14 kD (Spectrum), which were unremittingly agitated in an orbital shaking water bath at 37 ^{O}C. At specific time intervals, the release medium was taken out, and the new medium was replenished. The quantification of the released drug from the RTPLN and RTSLN was performed using a UV-Vis spectrometer (Shimadzu, UV-2700) at a wavelength of 257 nm. Additionally, drug release outlines were predictable by dialyzing in contradiction of PBS (pH 7.4) in the occurrence of 20% (v/v) FBS [42]. The dissolution study of RTPNs and RTSLNs was conducted using a USP Type II dissolution apparatus in an acidic phosphate buffer (pH 5.5) to simulate liver cancer cell conditions. Both formulations, equivalent

to 5 mg of rutin, were added to 900 ml of buffer at 37 ± 0.5 ^{O}C, with the paddle speed set at 100 rpm. Samples were withdrawn at regular intervals (0 to 6 hours), filtered, and analyzed using UV-Visible spectrophotometry at a λ_{max} of 358 nm. The drug release (% DR) for each sample was calculated, and the dissolution profiles of both formulations were compared to determine their performance under acidic conditions.

3.8 MTT assay

The cytotoxicity of RTPNS and RTSLNs was evaluated in vitro using an MTT (3-(4, 5-dimethylthiazol-2-yl)-2, 5-diphenyltetrazolium bromide) assay. Initially, cells were seeded in 96-well plates with flat bottoms, with a cell density ranging from 4000 to 5000 cells per well, and were then incubated at 37 ^{O}C for 24 hours. Subsequently, different concentrations of CPT-11, free Rutin, RTSLNs, and RTPNs-formulated nanoparticles were introduced to the cells, followed by an additional 72-hour incubation at 37 ^{O}C. After this incubation period, 30 μL of MTT solution (5 mg/mL in PBS) was applied to each well. Four hours later, the resulting purple MTT-formazan crystals were solubilized by adding 100 μL of DMSO. The absorbance in each well was predicted at 490 nm using a microplate reader (Multiskan FC, Thermo Scientific) [43].

3.9 Assessment of toxicity of nanoformulations

Cell toxicity was assessed using NIH3T3 mouse embryonic fibroblast cells. These cells were grown in Dulbecco's modified Eagle's medium, supplemented with 10% fetal bovine serum and 1% penicillin/streptomycin, and were maintained at 37 ^{O}C in a moistened incubator with 5% CO_2. Seeding was conducted in 96-well plates at a concentration of 10,000 cells/well. After a 24-hour incubation period, spent media was substituted with new media. Subsequently, samples of nano-formulations, specifically RTSLNs and RTPNs, were introduced, and the cells were incubated for 24, 48, or 72 hours. Control experiments that did not involve the addition of nanoparticles were also set up for comparative analysis. Cell viability was evaluated using Alamar Blue^{TM} assays from Biosource, which measure cell proliferation by detecting metabolic activities. To ensure the reproducibility of results, the experiments were repeated three times for each experimental condition [44].

3.10 Fluorescent cell studies

This method was used to determine the chromatin condensation by finding apoptotic cells. SLNPs and RTPNs treated with 96-well plates were used to grow cells (∼1 × 106 cells/mL) and incubated with Hoechst dye (16.23 mM solution 1:2000 in PBS) for 5 min. The dye binds mainly with the adenine (A) – thymine (T) rich DNA regions and produces blue fluorescence when excited by UV light at 350 nm. A negative control without nanoparticles is also tested in the same conditions [45].

3.10.1 Cell death assessment by (acridine orange/ethidium bromide) AO/EB fluorescence staining

HepG3B cells were propagated at a concentration of 0.5 to 2.0 million cells per milliliter and were incubated for 24 hours with synthesized RTPNs and RTSLNs. Trypsinization was then used to harvest the cells, and centrifugation was used to extract the resultant cell pellet. Before starting the process of microscopical quantification, 1 μL of AO/EB solution was used to stain the cell pellet, which was reconstituted in cold PBS. A quick assessment was done on the sample. Ten microliters of the cell solution were put on a microscope slide, sealed with a coverslip, and viewed under a fluorescence microscope fitted with a fluorescein filter and a 60X objective. In doing this investigation, almost 300 cells were observed [46].

3.10.2 HO (Hoechst assay for apoptotic nuclei)

This work used the Hoechst assay, which measures chromatin condensation to identify apoptotic nuclei. At a density of about one million cells per milliliter, cells were grown in 96-well plates that had been pre-treated with RTPNs and RTSLNs. After that, they were exposed to Hoechst dye (16.23 mM solution, diluted 1:2000 in PBS) for a duration of five minutes. When UV light is applied at 350 nm, the dye mostly attaches to DNA sections rich in adenine (A) and thymine (T), and it releases a blue fluorescence. The same experimental conditions were applied to the control sample with nanomedicines [46].

4. Results and discussions

4.1 Molecular interaction studies

The force field and minimization algorithm run on the proteins 5IZQ, 5ABD, and 4PZ3 resulted in a stable energy level of -110,394 kcal/mol, -17,200.20 kcal/mol, and 19,537 kcal/mol for and binding pocket algorithm generated the red color spherical binding pocket for all the three proteins shown in (Fig. 1 A, 1 B and 1 C) and the CHARMm-based docking protocol run resulted in the best binding possess of molecule in the cavity of all the three proteins. The docking of 8 bioactive molecules run showed that, the natural molecule Rutin formed the proper conformation by the active site amino acid with an affinity level of -44.5015 kcal/mol, -46.8331 kcal/mol, and -42.6949 kcal/mol for all

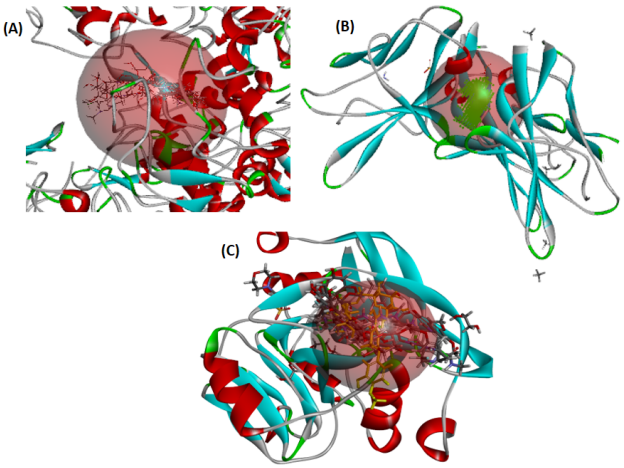

Figure 1. A. Secondary structure of protein 5IZQ with the binding pocket. B. Secondary structure of protein 4PZ3 with the binding pocket. C. Secondary structure of protein 5ABD with the binding pocket.

Table 4. Multiple energy parameters and the docking energy associated with the interactions between drug molecules and proteins.

Name	Initial potential energy	Initial RMS gradient	Electrostatic energy	Final potential energy	vdW energy	Final RMS gradient	Dock energy
5IZQ	-29,001	2,020.03	-113,874	-110,394	-11,386	1.07351	–
Curcumin	56.0782	34.5349	-40.9531	-24.9732	1.63772	0.00922	-22.9231
Hesperidin	265.266	40.5662	-32.2194	42.6945	-4.8129	0.00924	-17.7401
Lenvatinib	1,260.09	85.1318	-50.0869	-10.7878	8.4321	0.00941	-16.9617
Quercetin	71.9823	42.9541	-17.7776	-6.85907	1.69704	0.00999	-25.5015
Regorafenib	159.698	102.029	-42.8235	-13.9488	6.29573	0.00911	-30.8701
Resveratrol	45.5756	40.4805	-8.1863	2.4899	4.40981	0.00868	-27.8654
Sorafenib	145.157	79.9524	-32.2128	-4.50478	6.15224	0.00914	-31.1768
Rutin	650.295	550.589	-36.2585	-29.9889	79.4350	0.00909	-44.5015
5ABD	38,022.70	2,729.84	-17,431	-17,200.20	-2,031	1.19381	–
Curcumin	56.0782	34.5349	-40.9531	-24.9732	1.63772	0.00922	-6.50728
Hesperidin	265.266	40.5662	-32.2194	42.6945	-4.8129	0.00924	-33.6498
Lenvatinib	1,260.09	85.1318	-50.0869	-10.7878	8.4321	0.00942	-32.3458
Quercetin	71.9823	42.9541	-17.7776	-6.85907	1.69704	0.00999	-1.80832
Regorafenib	159.698	102.029	-42.8235	-13.9488	6.29573	0.00911	-20.2518
Resveratrol	45.5756	40.4805	-8.1863	2.4899	4.40981	0.00868	-7.65347
Rutin	650.295	550.589	-36.2585	-29.9889	-9.4350	0.00909	-46.8331
Sorafenib	145.157	79.9524	-32.2128	-4.50478	6.15224	0.00914	-20.4914
4PZ3	-9,314.01	35.1472	-20,150.50	-19,537	-2038.58	0.96438	–
Curcumin	56.0782	34.5349	-40.9531	-24.9732	1.63772	0.00922	-4.31644-
Hesperidin	265.266	40.5662	-32.2194	42.6945	-4.8129	0.00924	-1.43313
Lenvatinib	1,260.09	85.1318	-50.0869	-10.7878	8.4321	0.00941	-5.75118
Quercetin	71.9823	42.9541	-17.7776	-6.85907	1.69704	0.00999	-6.86304
Regorafenib	159.698	102.029	-42.8235	-13.9488	6.29573	0.00911	-9.46703
Resveratrol	45.5756	40.4805	-8.1863	2.4899	4.40981	0.00868	-16.7463
Rutin	650.295	550.589	-36.2585	-29.9889	-9.4350	0.00909	-42.6949
Sorafenib	145.157	79.9524	-32.2128	-4.50478	6.15224	0.00914	-11.9874

the given three proteins tabulated in (Table 4).

The natural molecule Rutin formed 6 different categorized interactions inside the binding pocket of the 5IZQ receptor illustrated in (Fig. 2 A). Totally 4 active site amino acids formed conventional hydrogen bonds with the oxygen and hydrogen atoms of the Rutin molecule and ARG F: 39 formed carbon-hydrogen bonds with the atoms of the Rutin molecule. Similarly, alkyl interactions were formed by PRO F: 194 amino acid, and π σ interaction generated with the LYS D: 30 significantly played a role in binding with a final dock energy of -44.5015 tabulated in (Table 4). The Rutin molecule generated 6 different categorized interactions inside the binding pocket of the 5ABD receptor illustrated in (Fig. 2 B). A total of 9 active site amino acids formed conventional hydrogen bonds with the oxygen and hydrogen atoms of the Rutin molecule, and three amino acids LYSA : 171, PROB : 173, and GLYA : 203 formed 6 carbon-hydrogen bonds with the atoms of the Rutin molecule. Similarly, Vander Waals interactions were formed by 12 amino acids, and three different kinds of π interactions were generated by TYRA: 199, ILEC: 142, and LYSB : 200 amino acids. Fig. 2 C explicated the best binding molecule of Rutin with protein 4PZ3 making more than 12 interactions. And four kinds of networks with active site amino acids. Specifically, the conventional hydrogen bond interaction created between ASNB : 120, PHEB 56,

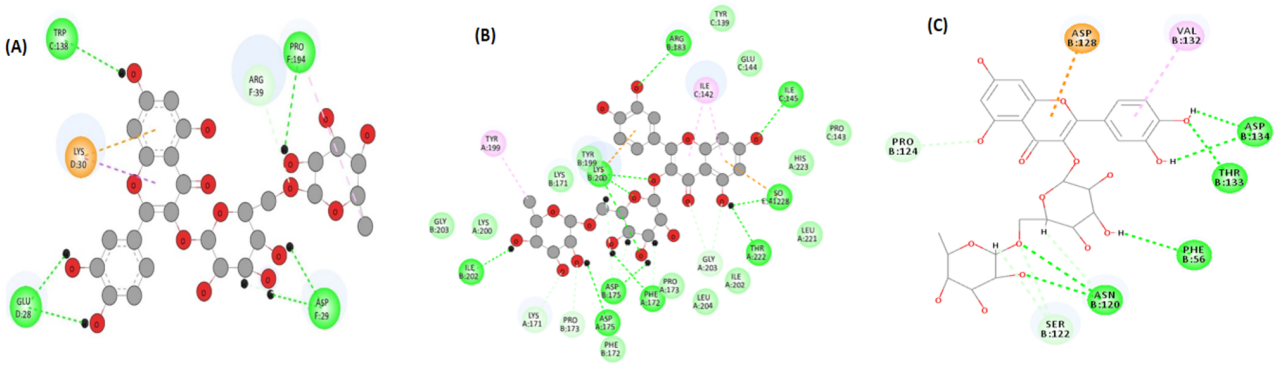

Figure 2. A. Interaction of active site amino acids of the protein 4PZ3 with Rutin B. Interaction of energetic site amino acids of the protein 5ABD with best-interacting molecule Rutin. C. Interaction of active site amino acids of 4PZ3 with best-interacting molecule Rutin.

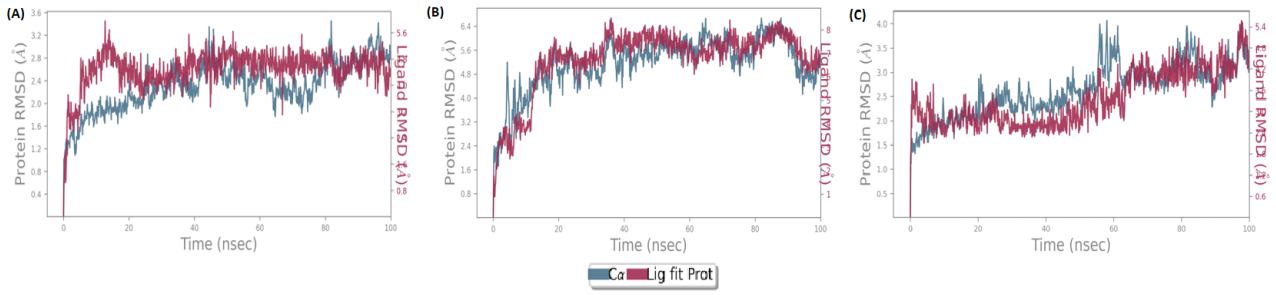

Figure 3. Molecular dynamics simulations outcomes of Protein-ligand interactions. (A) RMSD of natural molecule Rutin with 5IZQ protein receptor; (B) RMSD interaction of Rutin with 5ABD protein receptor. (B) RMSD between 4PZ3 protein receptor and Rutin molecule.

THRB : 133, and ASPB : 134 with hydrogen and oxygen atoms of Rutin. The carbon-hydrogen bond was generated with amino acids PROB : 124 and SERB : 122 in addition π-anionic and alkyl bonds were formed by two amino acids VALB : 132, and ASPB : 128 with the aromatic ring of Rutin. The Rutin molecule validated a remarkable ability to engage in diverse and specific interactions within the binding pockets of all three receptors, namely 5IZQ, 5ABD, and 4PZ3. These findings highlight Rutin's potential as a highly effective binding compound, supported by a variety of interaction types, further underlining its impending value in various biomedical applications and drug development.

4.2 Molecular dynamics studies

4.2.1 Protein-ligand RMSD for 5IZQ, 5ABD, and 4PZ3 proteins

The root mean square deviation (RMSD) analysis of the simulation runs between the 5IZQ, 5ABD, and 4PZ3 proteins with Rutin molecule. Fig. 3 A elucidates that the protein 5IZQ and Rutin molecule start stabilizing at the time of 16 ns and completely stabilizing at 42 ns. Similarly, with 5ABD, the molecule starts stabilizing at the time of 35 ns and up to the complete simulation run Fig. 3 B. Finally, with 4PZ3 Fig. 3 C illustrates that the protein and Rutin molecule starts stabilizing at the time of 7 ns and completely stabilizing at 62 ns. The outcomes ratify that Rutin forms the high-alleviating compound with all three proteins. The results confirm that Rutin forms the more stable complex with all three proteins. The observed RMSD patterns indicate that Rutin's interactions with these proteins lead to progressively more stable conformations.

4.2.2 Protein-Ligand RMSF for 5IZQ, 5ABD, and 4PZ3 proteins

The root mean square fluctuations (RMSF) of the amino acids are shown in (Fig. 4 A, 4B, and 4 C). The Protein 5IZQ of amino acids fluctuation proved that the residues 18, 50-54, 58.72-74, 77-80,85, 91-95, 97-99,105, 128-132, 165-168 modified the energies of a complete complex of protein after binding with the Rutin molecule elucidated in (Fig. 4 A). Also changes the folding of protein to form stable Rutin – 5IZQ conformations. Fig. 4 B revealed the protein 5ABD amino acids fluctuation proved that the residue 15, 38-40, 41-47, 65-67, 70-74, 88-94, 136-140, 142, 144, 147, 160-165, 167, 188-190, 195-202, and 294 modified the energies of a complete complex of protein after binding with the Rutin molecule. Also changes the folding of protein to form stable Rutin – 5ABD conformations. Similarly, Fig. 4 C reveals that 4PZ3 amino acids fluctuation such as 103, 160, 165,1 80-189, 249-256, 259-261, 262-265, 267-270, modified the energies of a complete complex of protein after binding with the Rutin molecule. Also changes the folding of protein to form stable Rutin – 4PZ3 conformations. The RMSF analyses confirmed that Rutin forms highly prominent complexes with all three proteins 5IZQ, 5ABD, and 4PZ3. These interactions were characterized by substantial fluctuations in energy for specific amino acid residues, which not only modified the overall energies of the protein complexes but also influenced the folding of the proteins. This insight emphasizes the potential of Rutin as a key constituent in stabilizing the conformations of these protein complexes and highlights its promise in various health applications.

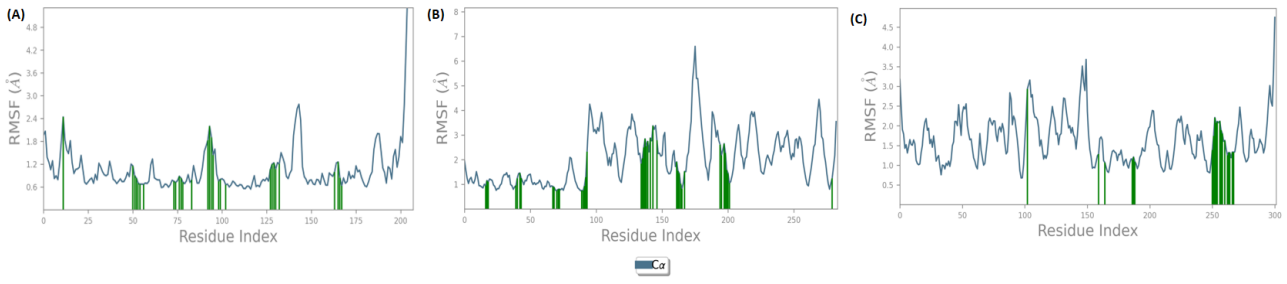

Figure 4. Molecular dynamics simulations effects of Protein-ligand interface. (A) RMSF of natural molecule Rutin with 5IZQ protein receptor; (B) RMSF of 5ABD protein receptor with drug molecule. (C) RMSF between the Rutin molecule and 4PZ3 protein receptor.

4.2.3 Ligand protein contacts for 5IZQ, 5ABD, and 4PZ3 proteins

The simulation interaction analysis depicted how Rutin establishes stable interactions with three different protein complexes 5IZQ, 5ABD, and 4PZ3. These interactions include the formation of hydrogen bonds, hydrophobic interactions, and ionic interactions, facilitated by the presence of water bridges. In the case of the 5IZQ complex, Rutin was observed to create these stable interactions by primarily engaging with the hydroxyl groups of the amino acids within 5IZQ, with water bridges serving as mediators mentioned in (Fig. 5 A & 5 B). The specific involvement of the amino acid ASP134 in the b-chain played a striking role, forming medium water bridges, small ionic interactions, and enduring hydrogen bonds. With 5IZQ comprising 20 amino acids, it becomes evident that Rutin binds to this complex effectively detailed in (Fig. S1).

For the 5ABD complex, similar stable non-bonded interactions involving hydrogen bonds, hydrophobic interactions, and ionic interactions were identified. The hydroxyl groups

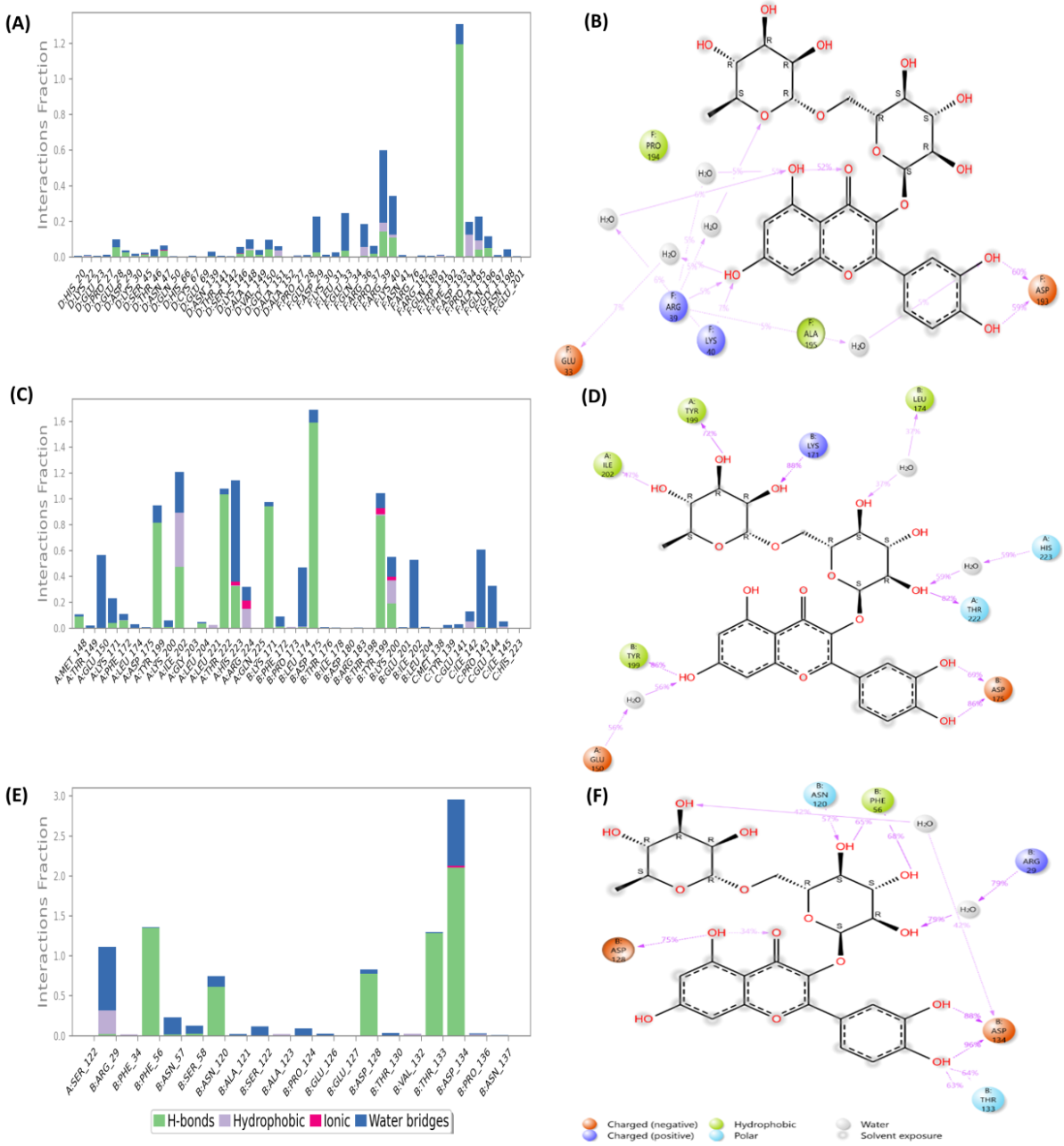

Figure 5. Molecular dynamics simulations outcomes of protein-ligand interaction histograms (hydrogen bonding, hydrophobic interactions, ionic interactions, and water bridges). (A) Histogram representation of the interaction of protein 5IZQ and Rutin molecule; (B) A structural illumination of detailed ligand atom Rutin interactions with the protein residues of 5IZQ. (C) Histogram illustration of the interaction of protein 5ABD and Rutin molecule; (D) A schematic of detailed ligand molecule Rutin interactions with the protein residues of 5ABD. (E) Histogram illustration of the interaction of protein 4PZ3 and Rutin molecule; (F) A structural elucidation of detailed ligand atom Rutin interactions with the protein residues of 4PZ3.

of Rutin again played a central role, mediated by water bridges that connected with the active sites of amino acids in 5ABD illustrated in (Fig. 5 C & 5 D). Approximately 40 amino acids were found to facilitate Rutin's binding, notably TYR199, LEU221, GUN225, and LEU174, which significantly contributed to stabilizing the secondary structure of the protein details given in (Fig. S2). In the case of the 4PZ3 complex, Rutin exhibited stable interactions characterized by hydrogen bonds, hydrophobic interactions, and ionic interactions, all facilitated by water bridges. The hydroxyl groups of Rutin played a pivotal role in these interactions with the active sites of amino acids in 4PZ3 elucidated in (Fig. 5 E & 5 F). Notably, more than 50 amino acids were involved in aiding Rutin's penetration and binding to the 4PZ3 protein more details are given in (Fig. S3). Rutin's ability to form stable interactions with these three distinct protein complexes, as elucidated through the simulation interaction illustrations, highlights its potential as an inhibitor of these proteins' activities. The connection of water bridges and the specific amino acids acknowledged in each complex shed light on the molecular mechanisms underpinning Rutin's actions, providing valuable insights for future research and claims in various biological contexts.

4.3 FTIR

4.3.1 RTSLNs

By using FTIR, nanoparticle surface chemistry and intermolecular interactions were characterized when rutin is incorporated in lipids. The principal lipid peaks in the RTSLN structure were depicted, as (Fig. 6) shows. O-H stretching vibrations are suggested by this peak in the high-wavenumber region which are frequent in flavonoids like rutin, which measures 3378.67 cm^{-1}. This peak can be attributed to glyceryl behenate as well as rutin presented in (Supplementary Fig. S4). The values 2913.91 cm^{-1} and 2852.2 cm^{-1}, are connected to C-H stretching vibrations in Glyceryl Behenate's alkyl groups. This peak of 2351.77 cm^{-1} could be associated with stretching vibrations of the C≡C triple bond due to its aromatic rings, rutin might have a role in this peak illustrated in (Supplementary Fig. S5). 1733.69 cm^{-1} peak is a sign of the ester functional group-specific C = O stretching vibrations. Glyceryl Behenate is probably the source of it. 1463.71 cm^{-1} is C - H bending vibrations are frequently seen in this range. Rutin and glyceryl behenate may potentially be the source of the peak. 1106.94 cm^{-1} . Peaks around 956.52 cm^{-1} are frequently connected to aromatic C - H bending vibrations, which may originate from rutin. A 533.221 cm^{-1} range of chemical vibrations is frequently present in the fingerprint region, where this peak is located (Supplementary Fig. S6). More precise information about the substances in the mixture or reference spectra would be needed for its interpretation.

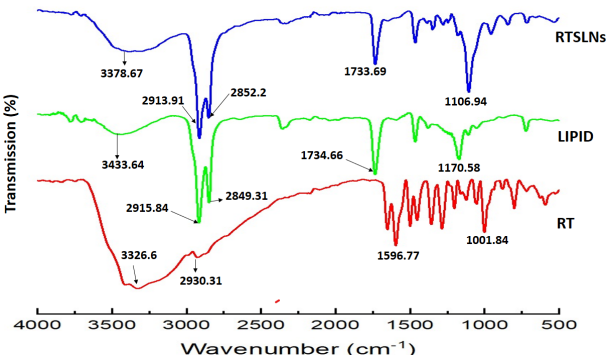

Figure 6. FTIR spectra Rutin in its pure form, the lipid compritol 888, and Rutin-loaded solid lipid nanoparticles (RTSLNs).

4.3.2 RTPNs

The peak observed at 3340.1 cm^{-1} signifies O-H (hydroxyl) stretching vibrations, indicating the presence of hydroxyl groups in Rutin. This observation also suggests that PDLG contains carboxylic acid (-COOH) groups as explicated in (Fig. 7). At 2919.7 cm^{-1}, we see a peak attributed to C - H stretching vibrations presented in (Fig. S7). These vibrations likely arise from the aliphatic portions of PDLG and the aliphatic (alkane) groups in Rutin. The peak at 1650.77 cm^{-1} resembles the C = O (carbonyl) stretching vibration, a characteristic feature of the carbonyl groups in PDLG and Rutin. The peak at 1597.73 cm^{-1} may be concomitant with the C = C stretching in the aromatic ring, a characteristic feature of flavonoids like Rutin, and it might also be present in PDLG. Moving on, the peak at 1355.71 cm^{-1} could be attributed to various functional groups present in both PDLG and Rutin, or it may be related to C - H bending vibrations. The peak at 1501.31 cm^{-1} could result from vibrations in C - H bending or C = C stretching in both PDLG and Rutin displayed in (Fig. S8). The peaks at 1287.25 cm^{-1} and 1002.8 cm^{-1} might be linked to functional groups in Rutin and PDLG or C-O stretching vibrations. The peaks at 800.314 cm^{-1} and 593.004 cm^{-1}, concomitant with out-of-plane bending vibrations, offer structural insights into the atomic arrangement in both PDLG and Rutin.

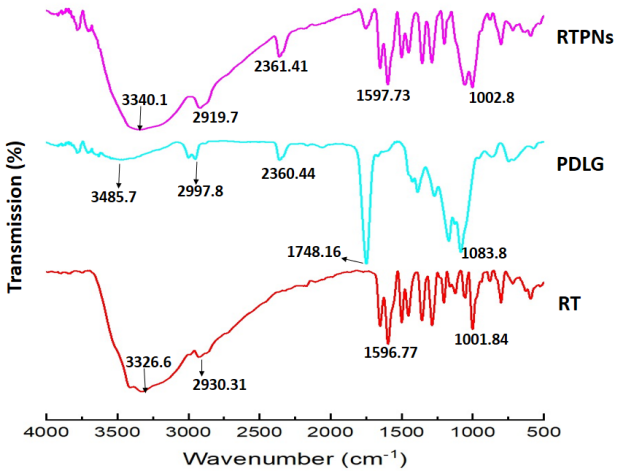

Figure 7. FTIR spectra were obtained for the following substances, Rutin in its pure form (RT), the polymer PDLG 5002A, and Rutin-loaded polymeric nanoparticles (RTPNs).

4.4 DLS and zeta potential

Both the RTPNs and RTSLNs formulations' A zeta potentials, which were determined to be -26.4 ± 0.4 and -25.5 ± 0.3 mv, respectively, suggested that the nanoparticles had a good degree of stability exemplified in (Fig. 8 A and

8 C) and (Supplementary file 1 & Supplementary file 2). Nanoparticles with negative zeta potential values tend to reject one another, which may assist in stopping them from aggregating. The particle size was generated as 58.31 ± 1.2 for RTSLNs and RTPNs 69.71 ± 1.5 nm was found virtuous within nanometers denoted in (Fig. 8 B and 8 D) and (Supplementary File 3 & Supplementary File 4). The PDI was found to be 0.294 ± 0.01 RTPNs and 0.268 ± 0.01 RTSLNs which is considered quite well and indicates a reasonably homogeneous distribution of particle sizes tabulated in Table 5. Furthermore, the concentration of the chosen surfactant and co-surfactant most likely decreased surface tension, which led to the creation of smaller nanoparticles.

4.5 TEM

To investigate the internal composition and surface characteristics of RTPNs and RTSLNs, transmission electron microscopy (TEM) analysis was conducted. The obtained Fig. 9 reveals that the nanoformulation particles exhibit nearly spherical shapes with smooth surfaces and fall within the nanoscale size range represented in (Fig. 9 B and 9 D). Specifically ranging from 46 to 70 nm for RTSLNs and

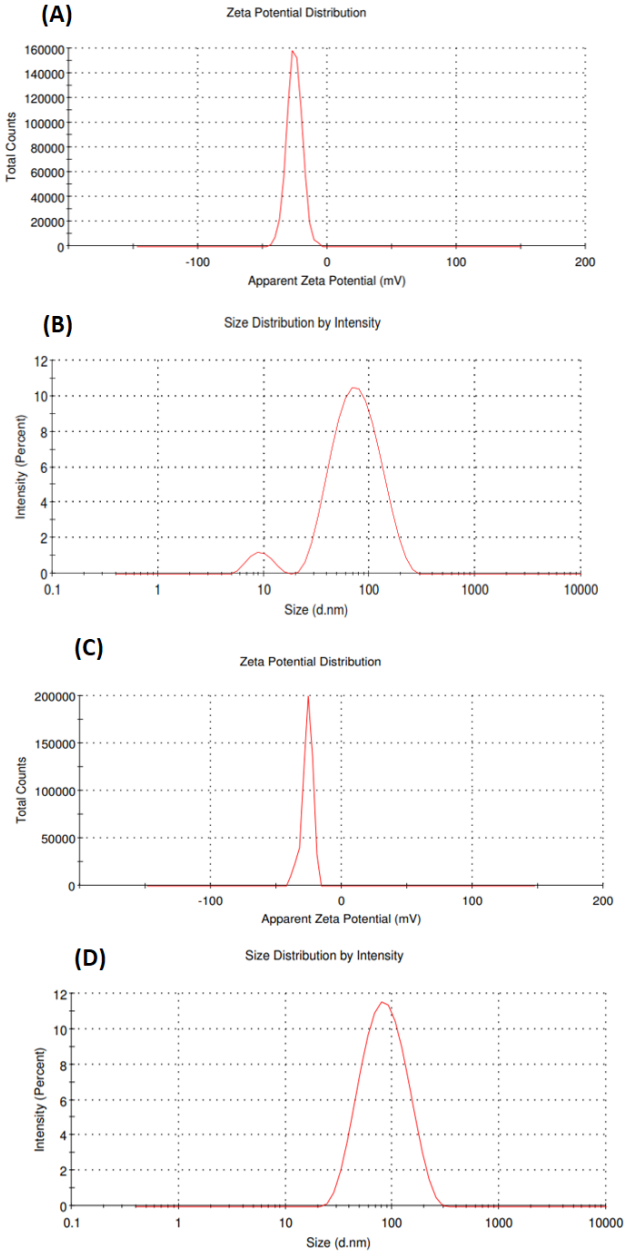

Figure 8. The nanoformulations were subjected to measurements of Z-average, PDI (Polydispersity Index), and Zeta Potential (ZP). These measurements were conducted in triplicate, with data presented as mean values along with their standard deviations (SD). (A) Zeta potential for RTPNs. (B) DLS of RTPNs. (C) Zeta potential for RTSLNs and (B) DLS of RTSLNs.

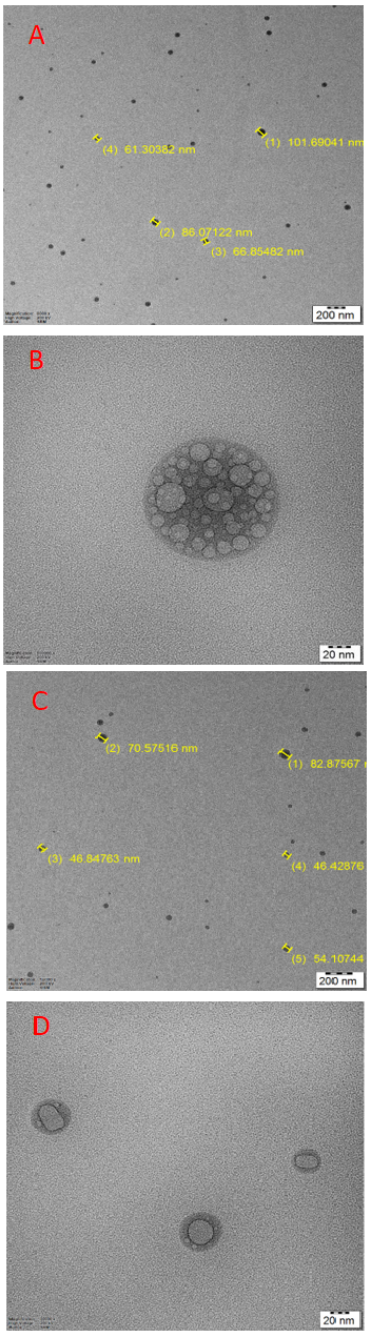

Figure 9. The formulations were subjected to transmission electron microscopy to investigate the following aspects (A) Providing a visual representation of the particle size distribution of RTPNs. (B) Analyzing the internal structure and surface characteristics of RTPNs. (C) offering a visual representation of the particle size distribution of RTSLNs. (D) Examining the internal structure and topographical features of RTSLNs.

Table 5. Particle size, PDI, and zeta potential of RTPNs and RTSLNs.

Formulation	Particle size (nm)	Polydispersity index	Zeta potential (mv)
RTPNs	69.71 ± 1.5	0.294 ± 0.01	-26.4 ± 0.4
RTSLNs	58.31 ± 1.2	0.268 ± 0.01	-25.5 ± 0.3

RTPNs ranging, from 61 to 101 nm illustrated in (Fig. 9 A and 9 C). Notably, all particles are observed to be uniformly distributed without any structural irregularities. The nanoparticles in RTPNs are larger in size when contrasted with RTSLNs (Fig. S9).

4.6 Drug loading (DL) and entrapment efficiency (EE)

The EE of RTSLNs is strikingly greater, at 82.61 ±1 .42%, and their standard deviation with a p-value of 0.001 is quite low. This high EE shows that the lipid nanoparticles may effectively and reliably encapsulate a significant amount of the medication. In distinction, RTPNs have a slightly greater standard deviation with a p-value of 0.002 along with a lower EE of 68.33 ± 2.29 % proven in (Fig. 10). Lipid and polymer nanoparticles have different structural and compositional properties, which account for the variations in EE. Lipid nanoparticles are a great option for drug delivery systems where efficiency, consistency, and stability are crucial since they continuously show higher EE with fewer standard deviations. When it comes to DL, lipid nanoparticles perform better than polymer nanoparticles. They have a DL of 10.74 ± 0.51 %, a p-value of 0.004 which is quite low, as opposed to a DL of 8.02 ± 0.95%, and a p-value of 0.008, polymer nanoparticles appear to contain less drug per unit of nanoparticles tabulated in (Table 6). This suggests that lipid nanoparticles can maintain a relatively low variance in drug loading while carrying a sizable amount of drug per unit of nanoparticles. The differences in Entrapment Efficiency (EE) and Drug Loading (DL) between RTSLNs (lipid-based nanoparticles) and RTPNs (polymer-based nanoparticles) are attributed to their structural properties. Lipid nanoparticles possess a flexible, hydrophobic core, allowing for better encapsulation of hydrophobic drugs like Rutin, leading to a higher EE (82.61 ± 1.42%) and DL (10.74 ± 0.51%) with lower variability. In contrast, polymer nanoparticles have a more rigid structure, limiting their drug encapsulation efficiency (68.33 ± 2.29%) and loading capacity (8.02 ± 0.95%). Lipid nanoparticles' reduced crystallinity, higher internal volume, and superior compatibility with hydrophobic drugs make them more effective for consistent drug delivery. Statistical significance in the data supports the hypothesis that lipid nanoparticles are more reliable for drug delivery systems, especially when efficiency and stability are critical.

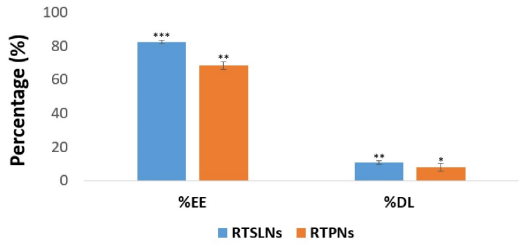

Figure 10. The entrapment efficacy (EE) and drug load (DL) of both RTSLNs and RTPNs formulations were assessed. An analysis of variance (ANOVA) was supported out to evaluate the significance of the modifications in EE and DL outcomes. These dimensions were performed in triplicate (n = 3 independent formulations), and the fallouts are offered as the mean values along with their conforming standard deviations (SD). Entrapment Efficiency (EE), RTSLNs have *** ($p < 0.001$), while RTPNs have ** ($p < 0.01$). For Drug Loading (DL), RTSLNs show ** ($p < 0.01$) and RTPNs show * ($p < 0.05$), confirming significant differences in drug encapsulation and loading between the two formulations. These results highlight that RTSLNs are the superior formulation, offering higher drug encapsulation and loading efficiency compared to RTPNs.

Table 6. Measurement of entrapment efficiency and drug loading capacity for RTPNs, and RTSLNs.

Formulation	Entrapment efficiency	Drug loading
RTSLNs	82.611 ± 1.42	10.743 ± 0.95
RTPNs	68.333 ± 2.29	8.017 ± 0.51

4.7 In vitro drug release

With a cumulative release that approaches 99% by the end of the dissolution, RTSLNs show a substantially greater drug release efficiency than RTPNs at all times. Additionally, RTSLNs have a remarkable ability to load drugs and transport them efficiently, as seen by their high cumulative drug release percentage of 99.222% at 6 hours and 96.93% at 5.5 hours illustrated in (Fig. 11 A). But after five hours, RTPNs fully released and show variations in their release kinetics, this suggests a less efficient and less regulated drug release mechanism. When it comes to therapeutic applications that need accurate dosing and consistent release, the variability in drug release from RTPNs raises questions about their dependability. When carefully examined from a scientific perspective, the dissolution data supports the claim that RTSLNs function better than polymer nanoparticles. RTSLNs nanoparticles provide great efficiency, stability, biocompatibility, and controlled and sustained release. For rutin, lipid nanoparticles are the recommended option due to these benefits and their great drug-loading capacity. The dissolution studies in acidic environment RTPNs exhibits rapid drug release, reaching near-complete dissolution (99.91%) by 4 hours, while RTSLNs demonstrates a slower, more sustained release, reaching 99.88% by 6 hours. RTSNP's pH-sensitive behavior at pH 5.5, mimicking acidic tumor conditions, indicates its potential for targeted cancer therapy. This gradual release profile ensures prolonged drug activity in the tumor environment, enhancing therapeutic efficacy. In contrast, RTPNs may be suited for scenarios requiring

a quicker, high-dose release. Overall, RTSNP's controlled release makes it a promising option for tumor-specific drug delivery (Fig. 11 B).

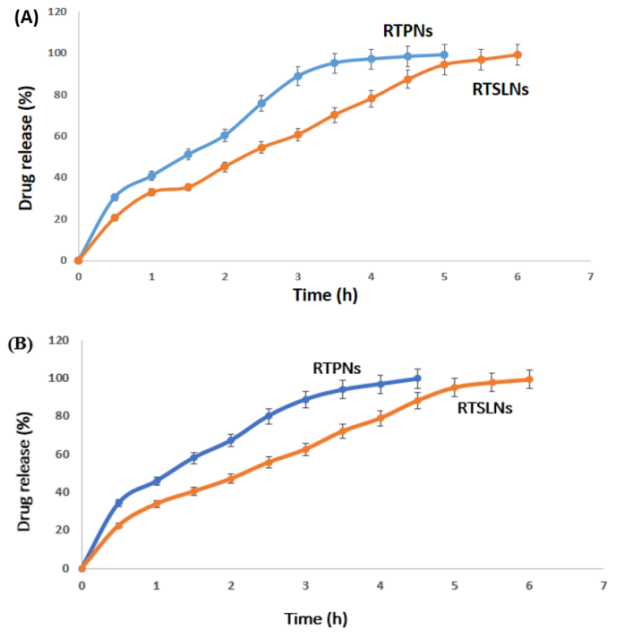

Figure 11. Drug release studies of (A) RTPNs and RTSLNs at various time intervals at pH 7.4, and (B) RTPNs and RTSLNs at different time intervals at pH 5.5.

4.8 MTT

The MTT screening outcomes reveal notable anticancer efficacy against HCC cell line Hep3B, for the nanoformulations fabricated using the Rutin-Loaded (RT) method. The IC50 value for RTSLNs was remarkably low at 80.45 ± 0.05 μg/mL proven in (Fig. 12 A). The lipid nanocarriers' effective transport of rutin, which improves penetration into the cell lines, is accountable for the substantial reduction in the IC50 value for RTSLNs. In contrast, RTPNs showed an IC50 that was comparatively larger at 120.45 ± 0.05 μg/mL, suggesting that their anticancer effect was not as strong as that of RTSLNs clarified in (Fig. 12 B). Additionally, pure Rutin showed the highest IC50 value of 160.15 ± 0.05 µg/mL shown in (Fig. 12 C) without the advantages of nanoparticle distribution, highlighting the beneficial impact of nanoformulations in boosting Rutin's therapeutic efficacy in the fight against HCC. These results highlight RTSLNs' promise as a viable platform for focused and efficient cancer treatment.

4.9 Statistical data for toxicity studies in NIH3T3 cell lines

The findings are reported as mean values with accompanying standard deviations, and the cellular reactions to the nanoparticles underwent statistical analysis through one-way analysis of variance (ANOVA). Cell viability experiments were conducted on NIH3T3 cell lines with an IC50 concentration of 80.45 ± 0.05 μg/mL for RTSLNs and 120.45 ± 0.05 μg/mL for RTPNs. The findings indicated that RTSLNs exhibited minimal toxicity, with mean values of 98.73 ± 0.49% live cells, while RTPNs showed a mean of 97.87 ± 0.35% at 24 hours. After 48 hours of treatment, the mean cell viability for RTSLNs was 95.67 ± 0.85%, and for RTPNs, it was 94.0 ± 0.74%. Subsequent treatment after 48 hours exhibited a diminution in cell viability, with values of 93.27 ± 1.16% for RTSLNs and 89.23 ± 1.29% for RTPNs depicted in (Fig. 13). The p-values for the comparison of control vs RTSLNs and control vs RTPNs were found to be 0.001 and 0.0002, respectively. The results indicate a higher percentage of cell death with RTPNs compared to RTSLNs, suggesting increased toxicity in NIH3T3 mouse embryonic fibroblast cells with RTPNs formulations compared to RTSLNs described in (Fig. 13) [44].

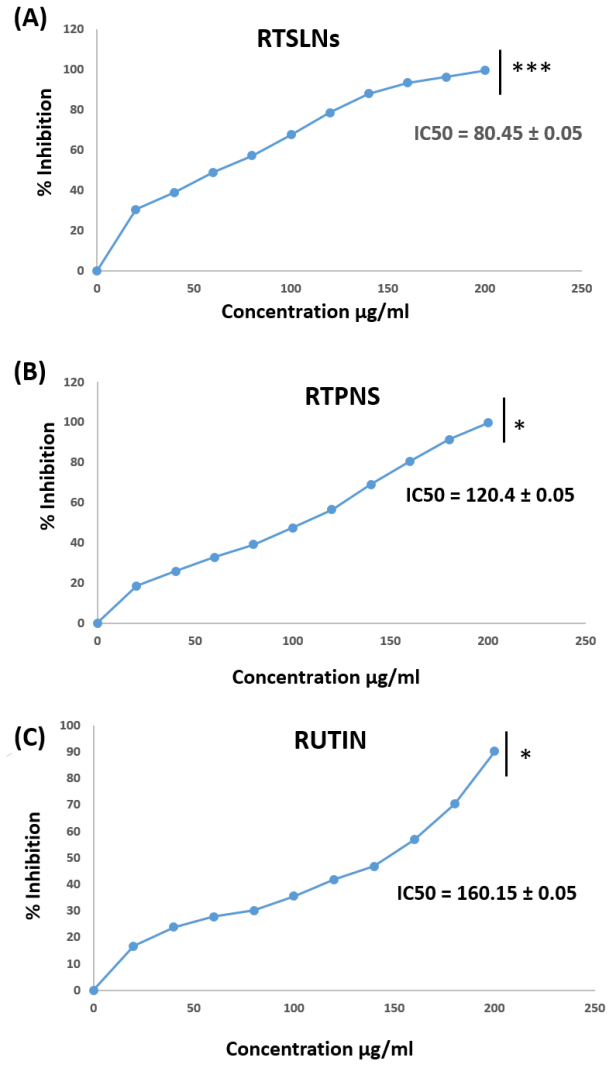

Figure 12. The MTT assay findings (screen-1) for the following categories. (A) Pure Rutin revealed in 160.15 ± 0.05 μg/mL (B) RTPNs (Rutin-loaded polymeric nanoparticles) exposed 120.45 ± 0.05 μg/mL. (C) RTSLNs (Rutin-loaded solid lipid nanoparticles) with IC50 value 80.45 ± 0.05 μg/mL. Based on the IC50 values, the approximate p-values are as follows: between RTSLNs and Rutin ($p < 0.001$), used *** (triple asterisks), while between RTSLNs and RTPNS ($p \approx 0.01$–0.05), and between RTPNS and Rutin ($p \approx 0.01$–0.05), used * (single asterisk) for both comparisons

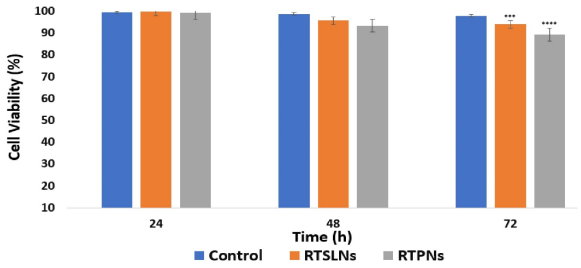

Figure 13. The toxicity studies of nanoformulation RTSLNs and RTPNs formulations were assessed. An analysis of variance (ANOVA) was carried out to assess the significance of the differences in cell viability of NIH3T3 cell lines. The measurements were conducted in triplicate, representing three independent formulations (n = 3), and the results are presented as mean values attended by their equivalent standard deviations (SD). The toxicity studies reveal significant differences in cell viability between RTSLNs and RTPNs, with ANOVA showing ***($p < 0.001$) for RTSLNs and ****($p < 0.0001$) for RTPNs at 72 hours. RTSLNs demonstrated higher cell viability, indicating better biocompatibility and reduced toxicity. These results, measured in triplicate (n = 3) and expressed as mean ± SD, confirm RTSLNs as a safer and more effective nanoformulation for therapeutic applications.

4.10 Cell death assessment by (acridine orange/ethidium bromide) AO/EB fluorescence staining

The results obtained from the fluorescent-based assay demonstrated that RLSLNs significantly decreased the viability of Hep3B cells, leading to a notable cytotoxic effect with an IC50 value of 80.45 ± 0.05 μg/mL. These findings clearly indicate that RTSLNs induced a higher level of apoptosis compared to both RTPNs and the control group. Fig. 14 illustrates the fluorescence patterns, showing approximately 60% apoptosis at the concentration of 80.45 ± 0.05 μg/mL for RTSLNs and 40% apoptosis at the concentration of 120.45 ± 0.05 μg/mL for RTPNs after 24 hours of treatment shown in (Fig. 14). The viable cells exhibit consistent green fluorescence and contain nuclei with a well-organized structure. In contrast, as observed in the control group, RTSLNs show early apoptotic cells displaying green fluorescence and condensed chromatin around the nucleus in the form of bright green patches, notably with enlarged size, which indicates necrosis in the cells. RTPNs, on the other hand, exhibit late apoptosis, with cells emitting an orange fluorescence and nuclei containing condensed or fragmented chromatin. Cells in the early stages of apoptosis exhibit green fluorescence, indicating the presence of intact cell membranes. Nevertheless, due to the reduced integrity of the cell membrane, a fraction of acridine orange escapes, leading to the appearance of orange staining. During the advanced phases of apoptosis or necrosis, cells display a red glow as a result of the binding of ethidium bromide to DNA. The red fluorescence acts as a marker for damaged cell membranes in the late stages of cell death which was observed in RTSLNs [47].

4.11 HO (Hoechst assay for apoptotic nuclei)

The IC50 concentrations of 80 μg/mL for RTSLNs and 120 μg/mL for RTPNs were used to treat Hep3 B cells, and the results of the Hoechst 33258 staining assay at 24 hours revealed cytological changes in these cells. The observations indicated that RTSLNs induced a greater degree of apoptosis, characterized by dot-like chromatin, cytoplasmic blebbing, cytoplasmic vacuolation, bi-nucleation, and nuclear shrinkage when compared to both the control and RTPNs groups represented in (Fig. 15). These findings confirm that RTSLNs, owing to their high cellular uptake mechanisms, intracellular behavior, and drug payload release and localization, are better suited to induce apoptosis and elicit a more pronounced response than RTPNs.

4.12 Discussion

The findings from this study indicate that RTSLNs consistently outperform RTPNs in multiple aspects of drug delivery and efficacy, highlighting their superior performance in cancer therapy. RTSLNs show significantly higher EE (82.61 ± 1.42%) and DL (10.74 ± 0.51%) compared to RTPNs, which exhibit lower values of EE (68.33 ± 2.29%) and DL (8.02 ± 0.95%). These differences are attributed to the structural advantages of lipid nanoparticles, such as a flexible hydrophobic core that allows better encapsulation of hydrophobic drugs like Rutin, leading to a more efficient drug delivery system. The in vitro drug release studies clearly illustrate the superiority of RTSLNs, which achieve a controlled and sustained release of 99.88% over 6 hours, while RTPNs exhibit rapid and less controlled release, reaching near-complete dissolution (99.91%) by 4 hours. This sustained release from RTSLNs ensures prolonged drug activity, making them more suitable for targeted cancer therapy, particularly in acidic tumor environments. MTT assays

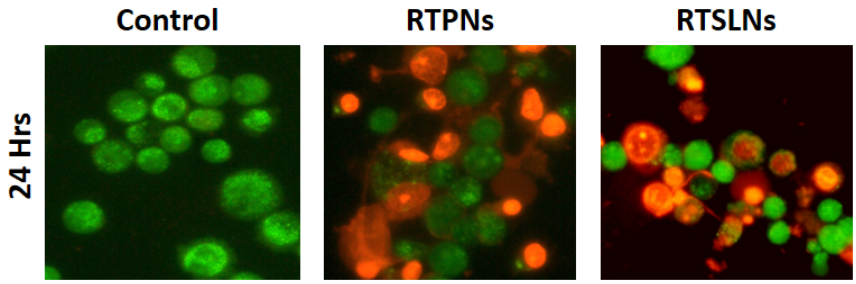

Figure 14. The apoptotic activity of the nanoformulations in Hep3 B cell lines at the 24-hour mark is as follows. Pure Rutin as the control, RTPNs (Rutin-loaded polymeric nanoparticles), and RTSLNs (Rutin-loaded solid lipid nanoparticles).

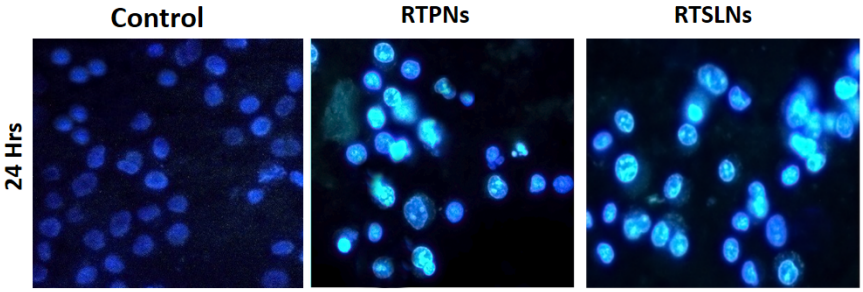

Figure 15. Hoechst assay for apoptotic nuclei in Hep3 B cell lines after a 24-hour period produced the following results for the nanoformulations. Pure Rutin as the control, RTPNs (Rutin-loaded polymeric nanoparticles), and RTSLNs (Rutin-loaded solid lipid nanoparticles).

show that RTSLNs are more effective in delivering Rutin to Hep3B liver cancer cells, with a significantly lower IC50 value (80.45 $\pm$ 0.05 μg/mL) compared to RTPNs (120.45 $\pm$ 0.05 μg/mL). This suggests that RTSLNs provide more effective drug penetration and cancer cell inhibition. Moreover, RTSLNs show lower toxicity to normal cells, as seen in NIH3T3 cell viability assays, where RTSLNs maintain higher viability compared to RTPNs, indicating better biocompatibility. In cell viability studies conducted on NIH3T3 cell lines, RTSLNs showed minimal toxicity with 98.73 $\pm$ 0.49% live cells after 24 hours and 95.67 $\pm$ 0.85% after 48 hours. In comparison, RTPNs exhibited slightly higher toxicity; with 97.87 $\pm$ 0.35% live cells after 24 hours and 94.0 $\pm$ 0.74% after 48 hours. After 48 hours, RTSLNs maintained higher cell viability (93.27 $\pm$ 1.16%) than RTPNs (89.23 $\pm$ 1.29%), indicating that RTSLNs are less toxic. Statistical analysis (ANOVA) showed significant differences with p-values of 0.001 for control vs RTSLNs and 0.0002 for control vs RTPNs, confirming that RTPNs induce more cell death, suggesting increased toxicity in comparison to RTSLNs. The AO/EB fluorescence staining and Hoechst assay results further confirm the enhanced apoptosis-inducing potential of RTSLNs. They lead to greater apoptotic cell death, as evidenced by significant chromatin condensation, cytoplasmic blebbing, and higher levels of apoptosis in cancer cells, compared to RTPNs. The controlled and sustained release profile of RTSLNs contributes to a more pronounced and effective apoptosis mechanism. Rutin-loaded RTSLNs effectively target malignant liver cells, potentially disrupting cell survival and proliferation pathways. This enhanced targeting and intracellular behavior underline their potential in cancer treatment, as RTSLNs ensure better drug localization and release within cancerous tissues, reducing off-target effects. Overall, RTSLNs demonstrate superior performance over RTPNs in terms of entrapment efficiency, drug loading, sustained release, anticancer efficacy, and biocompatibility. These advantages make RTSLNs the preferred nanoformulation for cancer therapy, offering enhanced therapeutic outcomes and reduced toxicity.

4.13 Summary of the molecular mechanism of Rutin-loaded nanoformulation

Rutin has been observed to interact with receptors present in malignant liver cells, potentially influencing signaling pathways related to cell survival, proliferation, or programmed cell death (apoptosis). This interaction warrants further exploration to determine whether Rutin directly impacts the behavior of malignant cells. Scientists frequently delve into the molecular mechanisms underlying the potential anti malignancy properties of natural compounds like Rutin through both in vitro and in vivo studies. As a result, the utilization of nanoformulations loaded with Rutin emerges as a promising approach. This method facilitates targeted delivery to tumor cells, minimizing potential harm to normal cells [48]. The molecular pharmacology illustrating how Rutin binds to and obstructs malignant cells is shown in (Fig. 16).

5. Conclusion

Indeed, HCC is a major global health risk that can be fatal. The most prevalent kind of primary liver cancer, HCC has a high fatality rate. Conventional chemotherapy's poor effectiveness and side effects have prompted research into alternative therapeutic strategies, such as anticancer drugs based on nanomedicine. Rutin has proven some possible health advantages, such as anti-inflammatory and antioxidant qualities. Rutin may protect the liver and be helpful in treating some liver disorders including HCC, according to some research and it is confirmed by *in silico* interaction and 100 ns dynamic simulation studies. Further, we fabricated the rutin-loaded polymeric and lipid nanoparticles to assess their therapeutic efficacies on HCC. When compared to rutin-polymeric NPs (PDLG), rt-LNs exhibit increased encapsulation efficiency (EE) and drug loading (DL) release characteristics. Furthermore, RTLNs display a more effective drug release behavior in comparison to RTPNs. In vitro cytotoxicity evaluations demonstrated that, in the instance of the Hep3B cell line, lipid NPs exhibited improved anticancer efficacy, with a lower IC50, in comparison to polymeric nanoparticles. The substantial anticancer properties of RT-loaded lipid nanoparticles were confirmed by further fluorescence screening, primarily by inducing death in Hep3B cells. Rutin interacts with receptors in malignant liver cells, potentially affecting signaling pathways. Further exploration is needed to assess Rutin's direct impact on cancer cell behavior. Scientists study Rutin's anti-cancer properties through in vitro and in vivo research. Utilizing Rutin-loaded nanoformulations shows promise for targeted delivery to tumor cells while minimizing harm to normal cells. According to these findings, SLNs—especially RT-

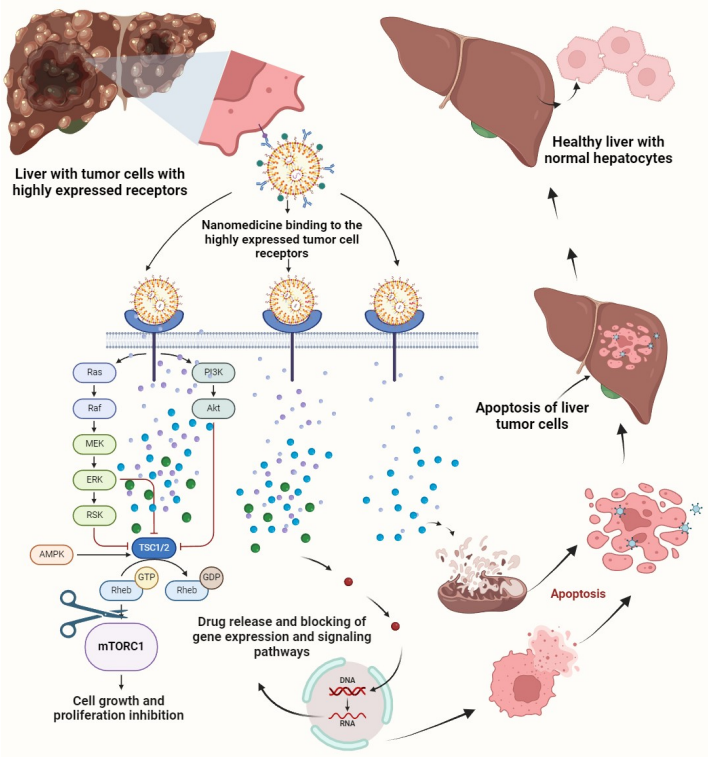

Figure 16. represents a brief overview of the molecular mechanism of Rutin-incorporated nanoformulation binding the highly expressed receptors and blocking the signaling pathways in liver malignant cells.

SLNs—have promise as nanoformulations that target HCC. It will take more research on relative bioavailability and in vitro/in vivo correlation research to compare and maximize the effectiveness of polymeric NPs and SLNs. Nonetheless, the study's findings suggest that these lipid NPs might have superior anti-malignancy action in HCC.

Authors contributions
Authors have contributed equally in preparing and writing the manuscript.

Availability of data and materials
The authors declare that the data supporting the findings of this study are available from the corresponding author upon reasonable request.

Conflict of interests
The authors assert that they do not have any identifiable conflicting financial interests or personal relationships that might be perceived to influence the work presented in this paper.

References

[1] B. Foglia, C. Turato, and S. Cannito. "Hepatocellular carcinoma: latest research in pathogenesis, detection and treatment.". *Int J Mol Sci*, 24, 2023.
DOI: https://doi.org/10.3390/IJMS241512224.

[2] M. Habeeb and A. Sugumaran. "Strategies of cell signaling and critical focus on etiology of hepatocellular carcinoma.". *Biointerface Research in Applied Chemistry*, 12:5187–5198, 2022.
DOI: https://doi.org/10.33263/BRIAC124.51875198.

[3] J. Chhatwal, A. Hajjar, P. P. Mueller, G. Nemutlu, N. Kulkarni, M. L. B. Peters, and F. Kanwal. "Hepatocellular carcinoma incidence threshold for surveillance in virologically cured hepatitis C individuals. ". *Clinical Gastroenterology and Hepatology*, 2023.
DOI: https://doi.org/10.1016/J.CGH.2023.05.024.

[4] N. Roehlen, M. Muller, Z. Nehme, E. Crouchet, F. Juhling, F. Del Zompo, S. Cherradi, F. H. Duong abd N. Almeida, A. Saviano, and M. Fernandez-Vaquero. "Treatment of HCC with claudin-1-specific antibodies suppresses carcinogenic signaling and reprograms the tumor microenvironment.". *Elsevier (n.d.).*, 2023.
DOI: https://doi.org/10.1081/AL-120006676.

[5] M. M. AbouSamra, S. M. Afifi, A. F. Galal, and R. Kamel. "Rutin-loaded Phyto-Sterosomes as a potential approach for the treatment of hepatocellular carcinoma: In-vitro and in-vivo studies.". *J Drug Deliv Sci Technol*, 79:104015, 2023.
DOI: https://doi.org/10.1016/J.JDDST.2022.104015.

[6] M. Ghanbari-Movahed, A. Mondal, M. H. Farzaei, and A. Bishayee. "Quercetin- and rutin-based nano-formulations for cancer treatment: A systematic review of improved efficacy and molecular mechanisms.". *Phytomedicine*, 97:153909, 2022.
DOI: https://doi.org/10.1016/J.PHYMED.2021.153909.

[7] M. Habeeb, H. Woon You, K. Balasaheb Aher, G. Balasaheb Bhavar, S. Suryabhan Pawar, and S. Dnyaneshwar Gaikwad. "Artificial neural networks for the prediction of mechanical properties of CGNP/PLGA nanocomposites.". *Mater Today Proc*, 2023.
DOI: https://doi.org/10.1016/J.MATPR.2023.08.354.

[8] T. Kareem. "Nanomedicine for targeting the lung cancer cells by interpreting the signaling pathways.". *Elsevier (n.d.).*, 14(1): 1–15, 2022. URL https://www.sciencedirect.com/science/article/pii/S1773224722007766.

[9] M. Habeeb, H. W. You, K. B. Aher, G. B. Bhavar, V. S. Khot, and S. Mishra. "Strategies of nanomedicine for targeting the signaling pathways of Colorectal cancer.". *J Drug Deliv Sci Technol*, 84: 104487, 2023.
DOI: https://doi.org/10.1016/J.JDDST.2023.104487.

[10] M. Habeeb, T. A. Kareem, K. L. Deepthi, V. S. Khot, Y. H. Woon, and S. S. Pawar. "Nanomedicine for targeting the lung cancer cells by interpreting the signaling pathways.". *J Drug Deliv Sci Technol*, 77, 2022.
DOI: https://doi.org/10.1016/j.jddst.2022.103865.

[11] V. Agrawal, R. Patel, and M. Patel. "Design, characterization, and evaluation of efinaconazole loaded poly(D, L-lactide-co-glycolide) nanocapsules for targeted treatment of onychomycosis.". *J Drug Deliv Sci Technol*, 80:104157, 2023.
DOI: https://doi.org/10.1016/J.JDDST.2023.104157.

[12] N. Zaghloul, A. A. Mahmoud, N. A. Elkasabgy, and N. M. El Hoffy. "PLGA-modified Syloid®-based microparticles for the ocular delivery of terconazole: in-vitro and in-vivo investigations.". *Drug Deliv*, 29:2117, 2022.
DOI: https://doi.org/10.1080/10717544.2022.2092239.

[13] M. Habeeb, H. T. Vengateswaran, H. W. You, K. Saddhono, K. B. Aher, and G. B. Bhavar. "Nanomedicine facilitated cell signaling blockade: difficulties and strategies to overcome glioblastoma.". *J Mater Chem B*, 2024.
DOI: https://doi.org/10.1039/D3TB02485G.

[14] B. Deepa, K. Gayathiridevi, M. Kalyan Chakravarthi, A. Shajahan, B. Shanti Sree, M. Imran Anees, and M. Habeeb. "Slow evaporation technique to grow 3 – Amino benzene sulfonic acid single crystal for Non-Linear optical (NLO) transmission.". *Mater Today Proc*, 62: 2119–2123, 2022.
DOI: https://doi.org/10.1016/j.matpr.2022.03.045.

[15] C. Hsu, P. Weng, and M. Chen et.al. "Therapeutic targeting of hepatocellular carcinoma cells with antrocinol, a novel, dual-specificity, small-molecule inhibitor of the KRAS and ERK oncogenic signaling.". *Elsevier (n.d.)*, 2023. URL https://www.sciencedirect.com/science/article/pii/S0009279722005385.

[16] B. Hou, L. Qin, L. H. B., and B. "Hepatocellular carcinoma cells as the model for developing liver-targeted RNAi therapeutics.". *Research, undefined 2023, , Elsevier (n.d.).*, 2023. URL https://www.sciencedirect.com/science/article/pii/S0006291X23000190.

[17] S. Kumar and A. P. C. "Potential molecular targeted therapy for unresectable hepatocellular carcinoma.". *Mdpi.Com (n.d.).*, 2023. URL https://www.mdpi.com/2078454.

[18] D. Bekric, M. Ocker, C. Mayr, and S. Stintzing. "Ferroptosis in hepatocellular carcinoma: mechanisms, drug targets and approaches to clinical translation.". *Mdpi.Com*, 2022.
DOI: https://doi.org/10.3390/cancers14071826.

[19] N. Pavlovic. "Targeting ER stress in the hepatic tumor microenvironment.". *Wiley Online Library*, 2021.
DOI: https://doi.org/10.1111/febs.16145.

[20] O. Daoui, H. Nour, O. Abchir, S. Elkhattabi, M. Bakhouch, and S. Chtita. "A computer-aided drug design approach to explore novel type II inhibitors of c-Met receptor tyrosine kinase for cancer therapy: QSAR, molecular docking, ADMET and molecular dynamics simulations.". *J Biomol Struct Dyn*, 2022.
DOI: https://doi.org/10.1080/07391102.2022.2124456.

[21] N. Mokgautsi, Y. Kuo, C. Chen, and Y. Huang. "Multiomics study of a novel naturally derived small molecule.". *Mdpi.Com (n.d.)*, 2023. URL https://www.mdpi.com/2073-4409/12/2/340.

[22] K. Sruthi, B. Anupama, N. L. Sudeepthi, P. G. Krishna, A. Kareem, and M. Habeeb. "Investigation of Wrightia tinctoria extract activity on Alopecia using In-silco and In-vivo studies.". *Res J Pharm Technol*, 15:643–649, 2022.
DOI: https://doi.org/10.52711/0974-360X.2022.00106.

[23] M. Habeeb, K. L. Deepthi, M. Vijaya Vara Prasad, N. Irfan, S. L. Ali, and K. Navyaja. "Development characterization and molecular swimulation studies of metoclopramide HCl and Tramadol HCl bilayer tablets,.". *Res J Pharm Technol*, 15:529–534, 2022.
DOI: https://doi.org/10.52711/0974-360X.2022.00085.

[24] Y. Antonius. "Prediction of Aflatoxin-B1 (AFB1) molecular mechanism network and interaction to oncoproteins growth factor in hepatocellular carcinoma.". *Repository. Ubaya. Ac. Id*, 2022.
DOI: https://doi.org/10.22207/JPAM.16.3.29.

[25] Y. Zheng, S. Ji, and X. Li. "targets of Taraxacum mongolicum against hepatocellular carcinoma: network pharmacology, molecular docking, and molecular dynamics simulation analysis.". *Peerj.Com (n.d.)*, 2022. URL https://peerj.com/articles/13737/.

[26] B. Sadeghi. "Green synthesis of silver nanoparticles using seed aqueous extract of Olea europaea.". *International Journal of Nano Dimension*, 5:575–581, 2014.
DOI: https://doi.org/10.7508/IJND.2014.06.010.

[27] M. S. Sadjadi, B. Sadeghi, and K. Zare. "Natural bond orbital (NBO) population analysis of cyclic thionylphosphazenes, [NSOX (NPCl2)2]; X = F (1), X = Cl (2).". *Journal of Molecular Structure: THEOCHEM*, 817:27–33, 2007.
DOI: https://doi.org/10.1016/J.THEOCHEM.2007.04.015.

[28] " Study of the shape controlling silver nanoplates by reduction process.". *International Journal of Bio-Inorganic Hybrid Nanomaterials*, 1(33):33, 2012. URL http://sanad.iau.ir/en/Journal/ijbihn/Article/928474.

[29] B. Sadeghi, S. H. Ghammamy, Z. Gholipour, M. Ghorchibeigy, and A. A. Nia. "Gold/hydroxypropyl cellulose hybrid nanocomposite constructed with more complete coverage of gold nano-shell.". *Micro Nano Lett*, page 209–213, 2011.
DOI: https://doi.org/10.1049/MNL.2011.0036/CITE/REFWORKS.

[30] E. A. Fayed, Y. A. Ammar, M. A. Saleh, A. H. Bayoumi, A. Belal, A. B. M. Mehany, and A. Ragab. "Design, synthesis, antiproliferative evaluation, and molecular docking study of new quinoxaline derivatives as apoptotic inducers and EGFR inhibitors.". *JMoSt*, 1236:130317, 2021.

[31] Y. A. Ammar, A. M. Sh El-Sharief, A. Belal, S. Y. Abbas, Y. A. Mohamed, A. B. M. Mehany, and A. Ragab. "Design, synthesis, antiproliferative activity, molecular docking and cell cycle analysis of some novel (morpholinosulfonyl) isatins with potential EGFR inhibitory activity.". *Eur J Med Chem*, 156:918–932, 2018.
DOI: https://doi.org/10.1016/J.EJMECH.2018.06.061.

[32] M. R. Bauer and M. D. Mackey. " Electrostatic complementarity as a fast and effective tool to optimize binding and selectivity of protein-ligand complexes.". *J Med Chem*, 62:3036–3050, 2019.
DOI: https://doi.org/10.1021/ACS.JMEDCHEM.8B01925/SUPPL_FILE/JM8B01925_S

[33] I. Navabshan, B. Sakthivel, R. Pandiyan, M. G. Antoniraj, S. Dharmaraj, V. Ashokkumar, K. S. Khoo, K. W. Chew, A. Sugumaran, and P. L. Show. "Computational lock and key and dynamic trajectory analysis of natural biophors against COVID-19 spike protein to identify effective lead molecules.". *Mol Biotechnol*, 63:898–908, 2021.
DOI: https://doi.org/10.1007/S12033-021-00358-Z.

[34] N. Irfan, S. Balasubramaniyan, D. M. Ali, and A. Puratchikody. "Bioisosteric replacements of tyrosine kinases inhibitors to make potent and safe chemotherapy against malignant cells.". *J Biomol Struct Dyn*, 2022.
DOI: https://doi.org/10.1080/07391102.2022.2146751.

[35] A. M. Omar, A. S. Aljahdali, M. K. Safo, G. A. Mohamed, and S. R. M. Ibrahim. "Docking and molecular dynamic investigations of phenylspirodrimanes as cannabinoid receptor-2 agonists.". *Molecules*, 28:44, 2023.
DOI: https://doi.org/10.3390/MOLECULES28010044/S1.

[36] T. Feczko, A. Piiper, T. Pleli, C. Schmithals, D. Denk, S. Hehlgans, F. Rodel, T. J. Vogl, and M. G. Wacker. "Theranostic sorafenib-loaded polymeric nanocarriers manufactured by enhanced gadolinium conjugation techniques.". *Pharmaceutics*, 11(489):489 11, 2019.
DOI: https://doi.org/10.3390/PHARMACEUTICS11100489.

[37] M. C. O. Da Rocha, P. B. Da Silva, M. A. Radicchi, B. Y. G. Andrade, J. V. De Oliveira, T. Venus, C. Merker, I. Estrela-Lopis, J. P. F. Longo, and S. N. Bao. "Docetaxel-loaded solid lipid nanoparticles prevent tumor growth and lung metastasis of 4T1 murine mammary carcinoma cells.". *J Nanobiotechnology*, 18, 2020.
DOI: https://doi.org/10.1186/S12951-020-00604-7.

[38] H. M. Alhelal, S. Mehta, V. Kadian, V. Kakkar, H. Tanwar, R. Rao, B. Aldhubiab, N. Sreeharsha, P. Shinu, and A. B. Nair. "Solid lipid nanoparticles embedded hydrogels as a promising carrier for retarding irritation of leflunomide.". *Gels*, 9, 2023. DOI: https://doi.org/10.3390/GELS9070576.

[39] P. Pandey, M. Rahman, P. C. Bhatt, S. Beg, B. Paul, A. Hafeez, F. A. Al-Abbasi, M. S. Nadeem, O. Baothman, F. Anwar, and V. Kumar. "Implication of nano-antioxidant therapy for treatment of hepatocellular carcinoma using PLGA nanoparticles of rutin.". *J. Organomet. Chem.*, 13(849–870), 2018. DOI: https://doi.org/10.2217/NNM-2017-0306.

[40] H. Akel, R. Ismail, G. Katona, F. Sabir, R. Ambrus, and I. Csoka. "A comparison study of lipid and polymeric nanoparticles in the nasal delivery of meloxicam: Formulation, characterization, and in vitro evaluation.". *Int J Pharm*, 604:120724, 2021. DOI: https://doi.org/10.1016/J.IJPHARM.2021.120724.

[41] F. De Gaetano, M. C. Cristiano, V. Venuti, V. Crupi, D. Majolino, G. Paladini, G. Acri, B. Testagrossa, A. Irrera, D. Paolino, S. Tommasini, C. A. Ventura, and R. Stancanelli. "Rutin-loaded solid lipid nanoparticles: characterization and in vitro evaluation.". *Molecules*, 26:1039 26, 2021. DOI: https://doi.org/10.3390/MOLECULES26041039.

[42] P. Pandey, M. Rahman, P. C. Bhatt, S. Beg, B. Paul, A. Hafeez, F. A. Al-Abbasi, M. S. Nadeem, O. Baothman, F. Anwar, and V. Kumar. "Implication of nano-antioxidant therapy for treatment of hepatocellular carcinoma using PLGA nanoparticles of rutin.". *ACS Appl. Mater. Interfaces.*, 10:849–870, 2018. DOI: https://doi.org/10.2217/NNM-2017-0306.

[43] M. J. Ansari, M. Rahman, K. S. Alharbi, W. M. Altowayan, A. M. A. Ali, W. H. Almalki, M. A. Barkat, T. Singh, S. Nasar, M. H. Akhter, S. Beg, and H. Choudhry. "Hispolon-loaded liquid crystalline nanoparticles: development, stability, in vitro delivery profile, and assessment of hepatoprotective activity in hepatocellular carcinoma.". *ACS Omega*, 7:9452–9464, 2022. DOI: https://doi.org/10.1021/ACSOMEGA.1C06796/ASSET/IMAGES/LARGE/AO1C

[44] G. K. Das, P. P. Y. Chan, A. Teo, J. S. C. Loo, J. M. Anderson, and T. T. Y. Tan. "In vitro cytotoxicity evaluation of biomedical nanoparticles and their extracts.". *J Biomed Mater Res A*, 93:337–346, 2010. DOI: https://doi.org/10.1002/jbm.a.32533.

[45] Y. Manojkumar, S. Ambika, R. Arulkumar, B. Gowdhami, P. Balaji, G. Vignesh, S. Arunachalam, P. Venuvanalingam, R. Thirumurugan, and M. A. Akbarsha. "Synthesis, DNA and BSA binding, in vitro anti-proliferative and in vivo anti-angiogenic properties of some cobalt(III) Schiff base complexes.". *New Journal of Chemistry*, 43: 11391–11407, 2019. DOI: https://doi.org/10.1039/C9NJ01269A.

[46] A. Puratchikody. "Identification of Silver nanoparticle-shaping tridax procumbens phytoconstituent by theoretical simulation and experimental correlation.". *RJLBPCS*, 4(3):131, 2023. URL www.ijpsonline.com.

[47] A. Anilkumar and A. Bhanu. "In vitro anticancer activity of "Methanolic extract of papaya blackseeds" (MPB) in Hep G2 cell lines and its effect in the regulation of bcl-2, caspase-3 and p53 gene expression.". *Advances in Cancer Biology - Metastasis*, 4, 2022. DOI: https://doi.org/10.1016/j.adcanc.2021.100025.

[48] T. Zhou, H. Zhou, L. Tian, M. Tang, L. Wang, Y. Kang, T. Chen, X. Li, S. Wu, R. Xia, X. Huang, L. Peng, and W. Yin. "Pomegranate juice-containing serum inhibits migration of hepatocellular carcinoma cells and promotes apoptosis by induction of mitochondrial dysfunction.". *J Nutr Biochem*, page 109557, 2023. DOI: https://doi.org/10.1016/j.jnutbio.2023.109557.